Computers and Geotechnics 192 (2026) 107908

Contents lists available at ScienceDirect

Computers and Geotechnics

journal homepage: www.elsevier.com/locate/compgeo

Research Paper

A discrete element approach for simulating progressive fracturing in geothermal reservoirs via a new cohesive crack model

Fei Wang [a,*], Dehao Meng [b], Heinz Konietzky [c], Eleni Gerolymatou [a], Paul W.J. Glover [d], Ben-Guo He [e]

[a] Technische Universität Clausthal, Clausthal-Zellerfeld, Germany
[b] GFZ Helmholtz Centre for Geosciences, Telegrafenberg, Potsdam 14473, Germany
[c] Geotechnical Institute, TU Bergakademie Freiberg 09596 Freiberg, Germany
[d] School of Earth and Environment, University of Leeds, Leeds LS2 9JT, UK
[e] State Key Laboratory of Intelligent Deep Metal Mining and Equipment, Northeastern University, Shenyang, China

ARTICLE INFO

Keywords:
Thermal cracking
Crystalline rock
Underground thermal energy storage
Heating–cooling cycles
Numerical simulation

ABSTRACT

In fractured geothermal energy storage systems, repeated heating and cooling cycles and fluid interactions cause non-linear and non-monotonic fracture deformations, requiring sophisticated modeling of complex thermo-hydro-mechanical (THM) behaviors. This paper proposes a new cohesive crack model for the discrete element method (DEM), aiming to enhance the characterization of the entire fracturing process in rocks during loading–unloading-reloading while considering thermo-hydraulic conditions. Specifically, the model proposed allows for flexible adjustment of post-peak tension behavior and is able to capture the progressive evolution of fracture opening and closing under cyclic THM loadings. Validation of the new model was performed under a range of thermo-hydraulic conditions, confirming its ability to replicate diverse fracture behaviors, and offering a comprehensive solution to modeling the complex interplay of thermal, hydraulic, and mechanical factors influencing rock fractures in the context of geothermal energy storage and extraction systems.

1. Introduction

In regions with high heating demands during winter, the seasonal variation in solar energy supply creates a supply–demand mismatch, especially in high-latitude countries (Janiszewski 2019). Various Underground Thermal Energy Storage (UTES) systems (Janiszewski 2019; Hesselbrandt and Acuna 2022) address this issue by storing waste or low-carbon heat during summer for extraction during winter. Among these systems, the fractured thermal energy storage (FTES) system uses natural or artificially induced fractures (hydraulic fracturing) in low permeability rocks like granite for thermal energy storage and extraction, making it a viable and cost-efficient method (Hesselbrandt and Acuna 2022). The temperature evolution in the fractured rock formations can be considered as a cyclic process of cooling during energy extraction and heating during non-operational/re-injection periods. As heat is stored and extracted, thermal stresses can lead to progressive damage in the rock, which may result in deformation and the development of fractures (Huang et al. 2022). Consequently, during thermal fluid storage and extraction, the repeated heating–cooling effects on fractures and surrounding rocks can significantly influence the opening of these fractures.

Understanding the thermal effects in fractured geological formations is particularly challenging due to the inherent complexity of rock mechanics and the heterogeneity of natural fractures. Thermal contraction and expansion can initiate or propagate fractures, alter rock permeability, cause stress re-distributions, and affect heat transport processes within deep underground rock mass (Koltzer et al. 2023; Wang et al. 2023, Wang et al. (2024a)). Therefore, in crystalline rock formations targeted for geothermal storage projects, understanding and managing the thermo-mechanical interactions such as thermal contraction and expansion are crucial. These interactions can significantly influence the behavior of fractures, impacting the overall performance and longevity of geothermal storage-extraction systems.

Numerical modeling is essential in order to replicate the fracturing behavior in geothermal energy storage systems because of the complex interplay between the thermal, hydraulic and mechanical aspects of the system. The model should be able to reproduce the dynamic fracture evolution in crystalline rocks as thermo-hydro-mechanical coupled

* Corresponding author at: Technische Universität Clausthal, Clausthal-Zellerfeld, Germany.
E-mail addresses: fei.wang.1@tu-clausthal.de, fei.wang-ing@outlook.com (F. Wang).

https://doi.org/10.1016/j.compgeo.2026.107908
Received 24 September 2025; Received in revised form 16 December 2025; Accepted 5 January 2026
Available online 8 January 2026

process. Most importantly, it should be capable of replicating the entire fracturing process, including initiation, growth, and coalescence of multiple individual cracks, ultimately leading to the formation of macro-fracture networks. In this context, the discrete element method (DEM) is commonly employed for such complex simulations. The fracture initiation and propagation can develop along and/or within the rock blocks, controlled by predefined contact properties and constitutive laws. For crystalline rocks like granite, DEM simulations can represent them as dense assemblies of blocks that interact at their contacts in the Distinct Element Code (DEC) (Itasca 2022). Such DEC offers robust hybrid (continuum and discontinuum) simulation capabilities to model fractured rocks, which may be rigid or deformable (zoned), and may slide, rotate, move apart, or come together. Previous models (Wang et al. 2023, Wang et al. (2024b)) have illustrated that DEC is a powerful tool for investigating real-time damage in granite under thermal loading, predominantly inducing tensile failure along grain boundaries with low micro-tensile strength, initiating microscopic tensile cracks at the grain scale. These tensile cracks extend and propagate, eventually forming large macroscopic fractures that lead to rock damage and failure (Wang et al. 2020; Saadat and Taheri 2020).

In the DEM, it is important to incorporate non-linear constitutive laws to describe the interface behavior based on the concept of non-linear fracture mechanics (Broberg 1971). The Cohesive Crack Model (CCM) is widely used to analyze the fracture of both plain and composite structures, describing how cohesive stresses evolve as the separation between crack faces increases, eventually leading to complete detachment (Farahmand and Diederichs 2015, 2021; Cornetti et al. 2019). While previous CCMs have successfully simulated rock fracturing under simple mechanical or hydro-mechanical conditions (Kumar and Barai 2009a; Kazerani and Zhao 2014; Farahmand and Diederichs 2015; Liu et al. 2024), they were developed primarily by incorporating softening functions developed for concrete and may not adequately replicate the diverse post-peak softening behavior of different crystalline rock types under coupled thermo-hydro-mechanical (THM) loading. Modeling the complex behavior of geothermal reservoirs requires a fully coupled consideration of thermal, hydraulic, and mechanical processes. Recent advancements have utilized various numerical strategies to tackle this challenge. For instance, Bongole et al. (2019) employed a finite element-based THM coupling method to investigate EGS performance, highlighting how temperature change significantly impacts reservoir deformation. Moving toward discrete fracture representation, Li and Zhang (2023) developed a 3D thermoporoelastic model combining the finite volume method with the displacement discontinuity method (DDM). They successfully simulated fracture propagation and fluid circulation in the EGS Collab experiment, capturing the mixed tensile-shear failure modes induced by thermal and hydraulic loading. Furthermore, Tiedtke et al. (2024) recently proposed a novel DFN-DEM approach that couples 3DEC with DFN.Lab to simulate long-term rock mass behavior under glacial climate conditions. Their study demonstrates the capability of DEM-based workflows to handle complex THM interactions over geological time scales.

While these studies advance significantly the understanding of THM coupling at the reservoir scale, many still rely on simplified constitutive laws for the fracture interface itself. A more sophisticated mechanical constitutive model is required to accurately capture the progressive damage evolution, from crack initiation to post-peak softening, particularly one capable of accommodating the variability of softening functions in FTES scenarios. This study introduces a new cohesive crack model for rocks, which is integrated with the standard thermal and hydraulic coupling features of the 3D distinct element code (3DEC) (Itasca 2022) to address this need. The newly developed model enhances the predictive capabilities of the DEM code, enabling a more sophisticated analysis of progressive rock fracturing under the cyclic hydro-thermal loading conditions typical of geothermal storage and extraction. Consequently, the primary contributions of this work are summarized as follows:

- Development of a new cohesive crack model (CCM) capable of simulating progressive fracturing in crystalline rocks under heating–cooling and hydraulic loading cycles, overcoming the limitations of the existing linear or brittle contact models in 3DEC.
- Incorporation of a nonlinear stress–displacement softening relationship, with two self-defined softening parameters (c_1 and c_2), allowing flexible calibration for different rock types and fracture behaviors.
- Introduction of a critical displacement coefficient (λ_u) that scales the post-peak displacement according to crystalline rock type, element size, and thermo-hydro conditions, enabling generalized application to a broad range of geological environments.
- Successful implementation and coupling within 3DEC, ensuring compatibility and stability with the in-built thermal and hydraulic modules. The new model achieves comparable or better accuracy than the built-in models in thermo-mechanical (TM) and hydro-mechanical (HM) benchmarks.
- Extension of DEM applicability from conventional rock mechanics problems to realistic simulations of fracture evolution in geothermal energy storage and extraction systems, which involve repeated thermal and hydraulic cycling.

2. Joint constitutive law considering progressive fracturing

2.1. Cohesive cracking behavior and governing equations

Both intergranular and intragranular cracks can form within the rock material under external loading. The normal force acting on these cracks is exerted by the surrounding constraints, either due to thermal expansion or mechanical compression. Existing fractures under repeated heating and cooling cycles will undergo cyclic loading and unloading, leading to progressive increases or decreases in fracture width. Within 3DEC models, such behavior at the contact interface (opening, closure and sliding) should be effectively captured to better simulate the effects of these thermo-mechanical interactions. The cohesive zone approach can be employed to describe the nonlinear stress–strain behaviors within the Fracture Process Zone (FPZ) in order to effectively model the progressive failure of rocks. The FPZ serves as a bridging zone between the cracked and uncracked regions, characterized by partial material damage and interlocking. Despite this damage, the material in the FPZ retains the ability to withstand stress and transfer loads between the cracked surfaces (Farahmand and Diederichs 2015). The nonlinear behavior of the contact under various modes of loading can be characterized by the cohesive crack model (CCM) (Perng 1989; Planas et al. 2003; Tatone 2014; Kazerani and Zhao 2014)(see Fig. 1). The crack is assumed to propagate when the stress at the crack tip reaches the local strength of the material, and the stress gradually decreases with increasing crack displacement rather than falling abruptly to zero (Hillerborg et al. 1976). Considering the superposition effects of both tensile and shear behavior, the contact effective displacement (Kazerani 2013) can be expressed as

$$\delta_{eff} = \begin{cases} \sqrt{u^2 + s^2} & u \geq 0 \\ s & u < 0 \end{cases} \tag{2.1}$$

where u is the normal contact displacement, and s is the shear sliding magnitude over the contact surface, respectively. The parameter u is assumed to be positive when the contact undergoes opening.

The governing equation of the nonlinear elastic behavior ($u \leq u_p$) is the exponential traction-separation law (Xu and Needleman 1993; Kazerani et al. 2012), representing the decay of stiffness in the pre-failure state due to the progression of damage (Farahmand and Diederichs 2015). The stiffness reduction due to damage behavior before fracture initiation can be represented by a decaying factor defined as

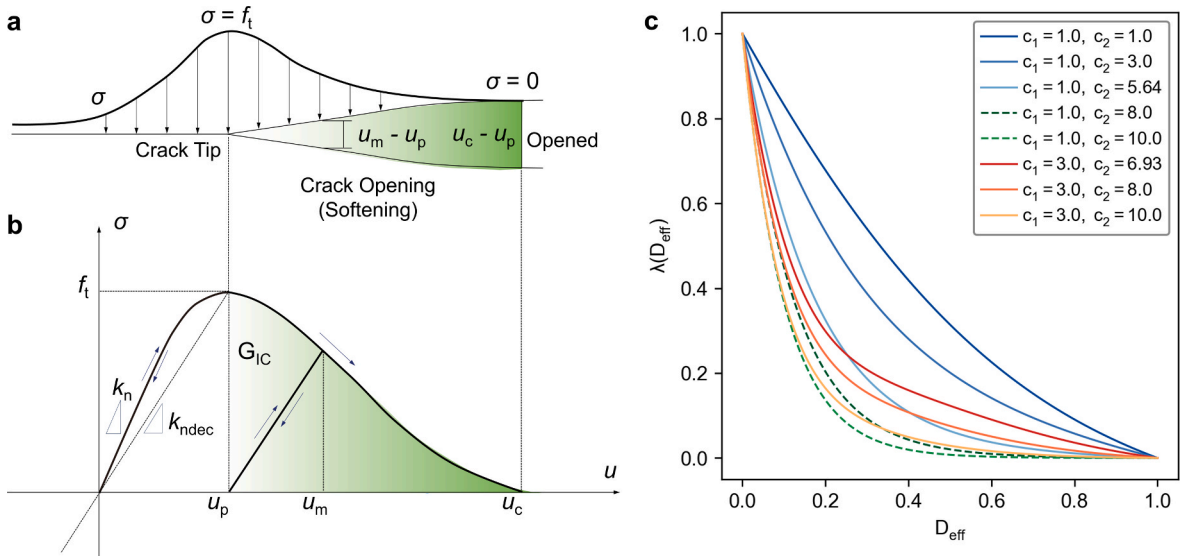

Fig. 1. Rock contact model considering nonlinear progressive fracturing. (a) Conceptual cohesive crack model of tensile loading. (b) Stress-displacement behavior of cohesive crack model (arrows denote loading, unloading and reloading paths). (c) Softening functions for different material constants.

$$\lambda_{decay} = e^{\left(-\frac{\delta_{eff}}{u_p}\right)} \tag{2.2}$$

where $e = exp(1)$ is the base of the natural logarithm, u_p is the contact normal displacement at peak stress beyond which cohesive softening occurs. Thus, contact is assumed to lose stiffness gradually upon opening to represent local material deterioration, and a non-linear relation is adopted to describe the pre-peak stress–displacement behavior of the contact. The contact cohesive stress in tension may be expressed as

$$\sigma = \begin{cases} k_n \cdot u \cdot \lambda_{decay} & u \le u_p \\ f_t \cdot \lambda(D_{eff}) & u = u_m,\ u_p < u < u_c \\ k_{ndec} \cdot u & u < u_m,\ u_p < u < u_c \\ 0 & u \ge u_c \end{cases} \tag{2.3}$$

where u_c is the critical contact tensile displacement at which the contact entirely loses its strength, u_m is the maximum displacement that u has reached during loading, thus, the interval $u_p < u < u_c$ represents the post-peak tensile stage before full separation, during which $u = u_m$ corresponds to the increasingly opening stage, whereas $u < u_m$ describes crack closure or reopening during unloading–reloading; k_n is the initial contact stiffness coefficient in tension, k_{ndec} is the decayed stiffness after peak, f_t is the contact tensile strength, $\lambda(D_{\text{eff}})$ is the softening function after fracture initiation, and D_{eff} is the contact effective damage coefficient ranging between [0,1]

$$D_{\text{eff}} = \begin{cases} 0 & \delta_{eff} \le u_p \\ 1 & \delta_{eff} \ge u_c \\ \dfrac{\delta_{eff} - u_p}{u_c - u_p} & u_p < \delta_{eff} < u_c \end{cases} \tag{2.4}$$

Crack tip peak stress occurs at $\sigma = f_t$ at $u = \delta_{eff} = u_p$, as shown in Fig. 1b. Substituting these values in Eq. (2.3), we obtain

$$f_t = k_n \cdot u_p \cdot e^{\left(-\frac{u_p}{u_p}\right)} = k_n \cdot u_p \cdot e^{-1}\ , \text{ and} \tag{2.5}$$

$$u_p = e \cdot \frac{f_t}{k_n} \tag{2.6}$$

The decayed stiffness can therefore be determined as

$$k_{ndec} = k_n \cdot e^{\left(-\frac{u_p}{u_p}\right)} = k_n \cdot e^{-1} \tag{2.7}$$

The initial contact stiffness coefficient in tension k_n before fracture initiation is often suggested to be taken as follows (Kazerani 2013; Kazerani and Zhao 2014)

$$k_n = \frac{E}{w} = \begin{cases} \dfrac{E^2 \sigma_t}{4K_{\text{IC}}^2} & \textit{plane stress} \\ \dfrac{E^2 \sigma_t}{4(1-\nu^2)K_{\text{IC}}^2} & \textit{plane strain} \end{cases} \tag{2.8}$$

where E is the Young's modulus of the undamaged material, and w is the thickness of the cohesive zone perpendicular to the orientation of crack propagation, ν is Poisson's ratio, K_{IC} is the critical value of stress intensity factor (i.e., fracture toughness), σ_t is the tensile strength. Plane strain conditions occur in long cylindrical bodies subjected to loads normal to the cylinder axis, whereas plane stress conditions occur in thin plates with traction-free surfaces (Gdutos 2020). For crack problems, plane strain conditions can be assumed for plates with a large thickness relative to the crack length, while plane stress conditions can be assumed in plates where the crack length is large compared to the plate thickness (Janssen et al. 2004). However, in this study the following relationship, as suggested for 3DEC (Itasca 2022), is used to determine the normal contact stiffness

$$k_n = N \bullet max\left[\frac{(K + \frac{4}{3}G)}{\Delta z_{min}}\right] \tag{2.9}$$

where K and G are the average bulk and shear moduli of the numerical elements, Δz_{min} is the smallest width of an adjoining zone (see Fig. 2b) in the normal direction, and N is usually smaller than 10 due to limitations on the maximum joint stiffness values that are practical in a 3DEC model. If N is more than 10, the solution time increases significantly without substantial impact on system behavior. In this study, N was set to 5 for granitic rocks, as adopted in previous studies (Wang et al. 2023, Wang et al. (2024b)).

Once yielding, the contact will undergo the softening stage ($u_p < u < u_c$). The shape of the post-peak gradual reduction of tensile stress σ acting on contact is governed by the softening function. The

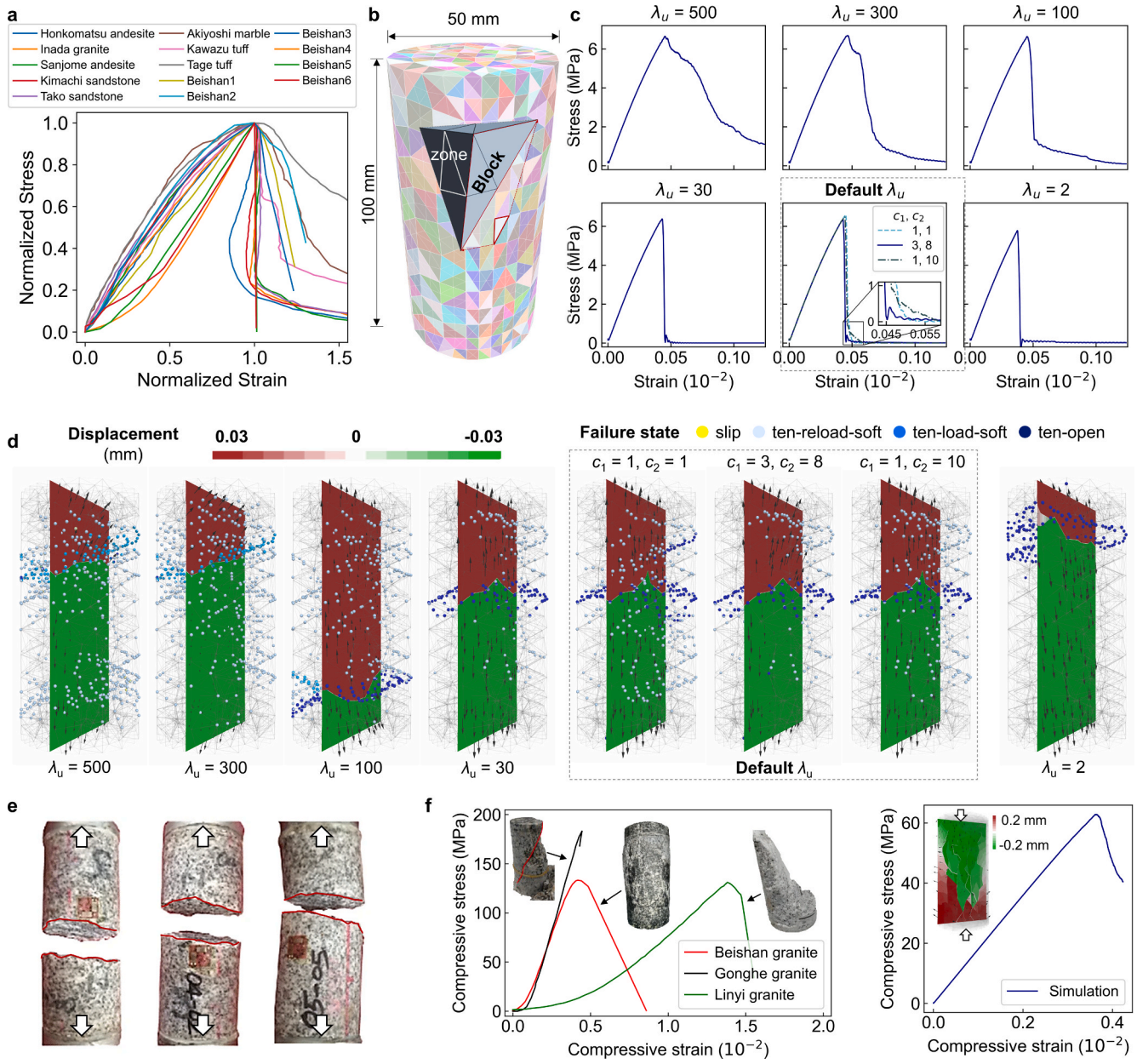

Fig. 2. Direct tensile behaviors of rocks obtained from laboratory testing and numerical simulations. (a) Normalized stress–strain curves from direct tensile tests on various rocks, data from literature (Okubo and Fukui 1996; Liu et al. 2020; Wang et al. 2022). (b) Cylindrical model for direct tensile test simulation with a close-up view of a single block. (c) Simulated stress–strain curves of direct tensile tests. (d) Final state of models under different λ_u after 30,000 calculation cycles ("ten" denotes tension failure, "slip" denotes shear failure, "load" and "reload" denote the loading and reloading stages, respectively, "soft" denotes the softening stage, "open" denotes fully open cracks). (e) Direct tensile results of the experimental Beishan granite samples (Liu et al. 2020). (f) Uniaxial compression results of the numerical model ($c_1 = 3.0$ and $c_2 = 8.0$, and default λ_u) and different experimental granite samples: Gonghe granite (Wang et al. 2024c), Beishan granite (Liu et al. 2020), Linyi granite (Cao et al. 2020).

global response and localized fracture behavior in the process zone and at the crack tip are affected by various shapes of softening functions. By comparing widely used softening functions such as linear, bilinear, exponential, quasi-exponential, and nonlinear, Kumar and Barai (Kumar and Barai (2009)) concluded that a nonlinear softening function (Reinhardt et al. 1986) offers higher accuracy than other types. Thus, the nonlinear softening function (Reinhardt et al. 1986) is introduced for this study

$$\frac{\sigma}{f_t} = \lambda(u) = \left[1 + \left(c_1 \frac{u - u_p}{u_c - u_p}\right)^3\right] e^{-\left(c_2 \frac{u-u_p}{u_c-u_p}\right)} - \frac{u - u_p}{u_c - u_p}(1 + c_1{}^3)e^{-c_2} \tag{2.10}$$

Substituting Eq. (2.4) into Eq. (2.10), the softening function can be obtained as follows

$$\lambda(D_{\text{eff}}) = \left[1 + (c_1 D_{eff})^3\right] e^{-(c_2 D_{eff})} - D_{eff}(1 + c_1{}^3)e^{-c_2} \tag{2.11}$$

where the coefficients c_1 and c_2 are material constants influencing the softening path. During the softening stage, energy release is allowed during unloading–reloading cycles. In unloading–reloading cycles ($u < u_m$), the contact follows a linear stress-displacement path where k_{ndec} is defined as the decayed stiffness at the point of crack initiation (see Fig. 1b). While a constant k_{ndec} is used in this implementation to ensure numerical stability during complex loading-reloading cycles, we

acknowledge that a more advanced formulation would feature an unloading stiffness that evolves with the current damage state, which remains a direction for future refinement.

Tensile failure is widely recognized as the primary driver of damage in rocks, while shear failure typically becomes significant only after substantial tensile damage has already occurred (Kazerani and Zhao 2014). Thermal cracking is predominantly manifested as tensile failure (Wang et al. 2023), indicating that thermal expansion and contraction mainly result in crack opening and closing. Hence, the key issue in geothermal storage and extraction processes is understanding the tensile response to thermal effects. For shear behavior related to temperature changes, the Coulomb slip model has proven to be effective in simulating thermal cracking in rocks (Woodman et al. 2021; Wang and Konietzky 2022; Wang et al. 2023). This model captures the displacement-weakening of joints by accounting for the reduction in cohesive strength and friction at the onset of shear failure. Shear stress on a joint develops according to the elastic model ($\tau = k_s \cdot s$) until reaching the peak strength f_s

$$f_s = c + \sigma_n tan\varphi \tag{2.12}$$

where c is cohesion, σ_n is the normal stress acting on the contact. The shear strength drops instantaneously to the residual shear strength when the peak shear strength is exceeded. Subsequently, the shear stress cannot exceed the residual strength. The residual strength f_{res} is given by

$$f_{res} = c_{res} + \sigma_n tan\varphi_{res} \tag{2.13}$$

After exceeding the shear strength, the joint may undergo dilation during shearing. The tangent of the dilation angle (ψ) indicates the amount of joint opening in the normal direction per unit of shear displacement for an unconfined joint. In real rocks, dilation is typically limited by large, accumulated shear displacements. Therefore, a critical shear displacement (s_c) is specified, beyond which no further dilation occurs (i.e., the joint may not continue to open indefinitely with increasing shear displacement) (Itasca 2022). Instead of explicitly modeling dilation as a physical displacement (in meters or millimeters), the dilation is represented as a normal force in 3DEC. This force is applied perpendicular to the joint surface in response to the shear displacement (i.e., the increase in aperture is considered as a force acting perpendicular to the shear direction, rather than just a physical displacement of the joint surfaces). If the joint is under compressive normal stress (acting to close the joint), the actual dilation (physical opening) will be less than what would be expected purely from the shear displacement. The applied force according to the amount of actual dilation is given by

$$\Delta\sigma_n = \begin{cases} k_n \bullet \Delta s \bullet tan\psi & s < s_c \\ 0 & s > s_c \end{cases} \tag{2.14}$$

It should be noted that the use of a constant dilation angle ψ is a simplification adopted for this study, which focuses primarily on tensile-dominated fracture behavior as seen in thermal cracking and hydraulic opening. For more complex, shear-dominated scenarios, such as fault reactivation, a more advanced law where ψ evolves with normal stress or damage would be necessary, and this remains a direction for future refinement. The newly developed constitutive model was first programmed in C++ and compiled into a dynamic link library (DLL) to optimize computational efficiency. This DLL was then integrated into 3DEC for the simulation of complex fracture mechanics under coupled THM conditions. Under tension, the model introduces a cohesive cracking *via* a nonlinear tensile stress-displacement relationship. A softening function governs the reduction of tensile stress after the peak. It effectively captures pre-peak and softening behavior by incorporating parameters like contact stiffness coefficients, tensile strength, and damage coefficients. Under shear loading, the model follows a Coulomb slip approach, which integrates joint stiffness, frictional properties, and dilation effects during shear failure. The complete model defines a comprehensive set of parameters, including normal stiffness (k_n), shear stiffness (k_s), cohesion, friction, tension, residual cohesion, residual friction, peak and critical displacements (u_p, u_c), and softening function parameters (i.e., material constants c_1, c_2).

2.2. Determination of softening function parameters c_1 and c_2

The softening parameter c_1 occurs, multiplied by D_{eff}, inside the cubic terms of Eq. (2.11), scaling the damage coefficient and amplifying the damage effect. A larger c_1 results in a more rapid initial decrease, causing the softening to reach lower values faster, as shown in Fig. 1c. The parameter c_2 is associated with the exponential decay term in Eq. (2.11), and moderates how the function behaves as D_{eff} approaches unity. Higher c_2 values cause the function to decay to lower values at higher D_{eff}. Therefore, according to the degree of damage, c_1 and c_2 determine the overall behavior of the softening curve: for small D_{eff}, c_1 predominantly influences the steepness and initial softening speed; for large D_{eff}, c_2 predominantly influences the decay rate. This controlling effect is important for different materials. As documented in the previous study (Kumar and Barai (2009)), values of $c_1 = 1.0$ and $c_2 = 5.64$ may be set for lightweight concrete, while $c_1 = 3.0$ and $c_2 = 6.93$ are set for normal-weight concrete. These c_1 and c_2 values result in a faster decay of the softening function after fracturing in normal-weight concrete. When addressing the behavior of crystalline rocks, the parameters should be adjusted to ensure that the cohesive law function demonstrates appropriate nonlinear behavior. Fig. 2a shows the stress–strain curves from direct tensile tests on various crystalline rocks. The post-peak stress decline varies significantly for different rocks. Some samples exhibit obvious ductile deformation prior to failure, while others lose their bearing capacity immediately upon reaching the peak stress. Additionally, some samples display an exponential weakening post-peak behavior.

In order to evaluate the influence of different pairs of c_1 and c_2 (the corresponding u_c is derived from Eq. (2.18) as shown in section 2.3) on the tensile stress-strains behaviors of granite models, simulations were conducted using three parameter sets: $c_1 = 1.0$ and $c_2 = 1.0$ ($u_c = u_p + \frac{2.644G_{IC}}{f_t}$), $c_1 = 1.0$ and $c_2 = 10.0$ ($u_c = u_p + \frac{9.946G_{IC}}{f_t}$), $c_1 = 3.0$ and $c_2 = 8.0$ ($u_c = u_p + \frac{6.324G_{IC}}{f_t}$). The model has a height of 100 cm and a diameter of 50 cm, comprising 2083 blocks with a zone edge length of less than 1 cm (see Fig. 2b). The specimen mesostructure, as illustrated in Fig. 2b, is generated by subdividing an initial intact block using a set of randomly oriented joint planes, creating an assemblage of interlocking convex polyhedral blocks (similar to a Voronoi tessellation). In this distinct element approach, the initial porosity of the rock matrix is assumed to be negligible (zero-porosity matrix), which is characteristic of dense crystalline rocks like granite. Consequently, the effective porosity and fluid flow are explicitly restricted to the network of contact planes (fractures). The model parameters are presented in Table 1. While c_1 and c_2 significantly influence the sub-contact stress–strain behavior (as shown in Fig. 1), their effect on the overall macro-behavior of the sample remains minimal (see Figs. 2c, d). This is because the macro-failure results from the cumulative effect of numerous sub-contact micro-failures. These micro-failures, despite being influenced by variations in c_1 and c_2, tend to average out at the macro-scale, resulting in a small impact on the overall behavior of the system. Therefore, in this study, considering a general crystalline rock, we set $c_1 = 3.0$ and $c_2 = 8.0$ as these values provide a balanced representation for combinations of different observed behaviors (see Fig. 1c and Fig. 2).

2.3. Determination of critical displacement u_c

The critical displacement u_c is often determined by solving the integral equations for fracture energy, since u_p can be calculated using f_t and k_n (see Eq. (2.6). For Mode-I cracking, the energy release rate G,

Table 1
Properties[†] of blocks and contacts (Preisig et al. 2015; Wang and Konietzky 2019; Wong et al. 2019; Tiedtke et al. 2024).

BLOCK and WATER											
ρ_s [kg/m^3]	E [GPa]	ν [-]	k^T [W/(m K)]	Cs [J/(kg K)]	α_T[1/K]	ρ_f [kg/m^3]	C_f [J/(kg K)]	h [W/m^2 K]	k_f^T [W/(m K)]	K_f[GPa]	η[Pa·s]
2700	50	0.25	2.5	1000	8.0×10^{-6}	1000	4180	2	0.6	2	1×10^{-3}
CONTACT											
k_n [Pa/m]	k_s [Pa/m]	φ [°]	φ_{res} [°]	c [MPa]	c_{res} [MPa]	ψ[°]	s_c[m]	f_t [MPa]	c_1 [-]	c_2 [-]	u_p [m]	u_c [m]	K_{IC} [MPa·m$^{1/2}$]
K, G (E, ν)	k_n/10	50* 30#	35* 30#	20×10^6* 0.1×10^6#	0.4×10^6* 0.1×10^6#	10 5#	5 u_c 5 u_c	10×10^6* 1.0×10^4#	3	8	$\frac{ef_t}{k_n}$	λ_u u_p	1.5

[†] Parameters are grouped by Block/Water and Contact properties. **Block and Water:** ρ_s is the solid (rock matrix) density; E is the Young's modulus; ν is the Poisson's ratio; k^T is the solid thermal conductivity; Cs is the solid specific heat capacity; α_T is the solid linear thermal expansion coefficient; ρ_f is the fluid (water) density; C_f is the fluid specific heat capacity; h is the convective heat-transfer coefficient; k_f^T is the fluid thermal conductivity; η is the dynamic fluid viscosity; K_f is the fluid bulk modulus. **Contact (Joint):** k_n is the joint normal stiffness; k_s is the joint shear stiffness; φ is the joint friction angle; c_{res} is the joint residual friction angle; c is the joint cohesion; c_{res} is the joint residual cohesion; ψ is the joint dilation angle; s_c is the critical shear displacement at which dilation ceases; f_t is the joint tensile strength; c_1, c_2 are the dimensionless material constants for the softening function (Eq. (2.11)); u_p is the contact normal displacement at peak tensile stress; u_c is the critical contact tensile displacement at which strength is lost; K_{IC} is the Mode-I fracture toughness.

[*] Represents intact rock.

[#] represents fracture. Strength parameters of fractures are set to low values to represent their inherent weakness and to accelerate the calculation speed during hydraulic fracturing simulations.

defined as the instantaneous loss of total potential energy per unit crack growth area, is related to the Mode-I stress intensity factor K_I by (Janssen et al. 2004)

$$G = \frac{K_I^2}{E'} \tag{2.15}$$

where E' is related to Young's modulus, E, and Poisson's ratio, ν, depending on whether the material is under plane stress or plane strain

$$E' = \begin{cases} E & \textit{plane stress} \\ \dfrac{E}{1-\nu^2} & \textit{plane strain} \end{cases} \tag{2.16}$$

Mode-I fracture energy G_{IC}, representing the energy required to fully open the unit area of a crack (Farahmand and Diederichs 2015), is thus defined by

$$G_{IC} = \begin{cases} \dfrac{K_{IC}^2}{E} & \textit{plane stress} \\ \dfrac{(1-\nu^2)K_{IC}^2}{E} & \textit{plane strain} \end{cases} \tag{2.17}$$

and

$$G_{IC} = \int_{u_p}^{u_c} f_t \cdot \lambda(D_{\text{eff}})\, du = f_t \int_{u_p}^{u_c} \left[\left(1 + 27\left(\frac{u-u_p}{u_c-u_p}\right)^3\right) e^{-8\left(\frac{u-u_p}{u_c-u_p}\right)} - 28e^{-8}\frac{u-u_p}{u_c-u_p} \right] du \tag{2.18}$$

By solving this equation, we can obtain

$$u_c = u_p + \frac{6.324 G_{IC}}{f_t} \tag{2.19}$$

Therefore, depending on whether the material is under plane stress or plane strain, the default critical opening value can take the following form:

$$u_c = \begin{cases} e\cdot\dfrac{f_t}{k_n} + \dfrac{6.324K_{IC}^2}{E \bullet f_t} & \textit{plane stress} \\ e\cdot\dfrac{f_t}{k_n} + \dfrac{6.324(1-\nu^2)K_{IC}^2}{E \bullet f_t} & \textit{plane strain} \end{cases} \tag{2.20}$$

However, this ideal relationship might not always be feasible for all types of crystalline rocks. Typically, the order of magnitude for f_t is 10^6 Pa, for k_n is 10^{13} Pa/m, for K_{Ic} is 10^6 Pa·m$^{1/2}$, and for E is 10^{10} Pa. Consequently, the order of magnitude for u_p is 10^{-7} m, while the calculated u_c is of the order of $10^{-5}/10^{-4}$ m. This results in u_c being much larger than u_p. As indicated in Fig. 2a, different crystalline rock types exhibit significantly different behavior in direct tension tests. Although some crystalline rocks lose strength completely after reaching peak stress, others retain a certain bearing capacity even after peak stress (Liu et al. 2014). Especially under THM conditions, the theoretical equation for calculating default u_c might not be applicable. Therefore, based on laboratory testing and simulation results, u_c may be set as

$$u_c = \lambda_u \bullet u_p \tag{2.21}$$

where the critical displacement scaling coefficient λ_u can be back-calculated, and may vary from 1 to 500 (see Fig. 2b), depending on rock type, element size, and THM conditions. To verify the effectiveness of this assumption, a series of direct tensile tests were performed with the 3DEC model, as shown in Figs. 2b, c, d. Fig. 2c shows the simulated stress–strain curves for models with different λ_u. The model with a λ_u of 500 exhibits a gradual loss of load-bearing capacity, similar to that of some rocks like marble (see Fig. 2a). As λ_u decreases, the rock material becomes more brittle. For λ_u below 30, the stress–strain curves display a sharp stress drop immediately after reaching the peak, with failure becoming more localized along a tensile fracture plane (see Fig. 2c). For crystalline rocks with $c_1 = 3.0$ and $c_2 = 8.0$, $u_c = u_p + \frac{6.324G_{IC}}{f_t}$ can be set as default. For rocks with unknown K_{Ic}, λ_u from 1 to 30 can be set to simulate the brittle tensile behavior of rock in a general way.

To validate the simulated failure mode, experimental crack patterns of Beishan granite produced under direct tension (Liu et al. 2020) are presented in Fig. 2e. The experimental results exhibit a macroscopic splitting fracture that aligns closely with the simulated failure pattern shown in Fig. 2d. While the default model effectively replicates the fundamental tensile failure mechanism, it should be noted that experimental fracture planes initiate stochastically within the gauge length due to material heterogeneity, rather than strictly at the geometric center. Consequently, further calibration of the softening parameters may be required to capture specific rock responses, particularly under varying temperature conditions. Beyond tensile behavior, the mechanical robustness of the model was further verified through a uniaxial compression simulation using the standard parameter set for crystalline rock (Table 1). Fig. 2f illustrates the resulting axial stress–strain curve and the final fracture pattern. The model exhibits a characteristic linear-

elastic response followed by a brittle stress drop upon reaching peak strength. The observed failure mode characterized by macroscopic shear fracturing and axial splitting is consistent with the typical brittle failure behavior of granites observed in experiments. It should be noted that the peak stress obtained is a result of the generic parameter set used in this study and was not calibrated to a specific granite sample; rather, these results serve to illustrate the model's inherent capability to simulate compressive failure mechanisms. This confirms that the newly proposed cohesive contact model, while optimized for tensile thermal fracturing, also correctly reproduces the fundamental constitutive behavior of the rock matrix under compression.

3. THM coupled model set-up

This study utilizes the in-built, standard thermal, hydraulic, and mechanical solvers of 3DEC, which are extensively documented and validated (Itasca 2022). The primary contribution of this work is not to redevelop these solvers, but to introduce the new cohesive mechanical model (Section 2) and verify its stable and accurate coupling with the existing THM framework. The 3DEC model assumes that the crystalline rock matrix is impermeable. Therefore, fluid flow and associated thermal transport are restricted to the fluid-filled fractures (the joint network). The solid blocks are modeled as deformable, discretized zones, which allows for the simulation of transient heat conduction and the development of thermal gradients within the blocks, leading to thermal-induced displacements and stresses. The following sections briefly outline the governing equations for this standard 3DEC coupling.

3.1. Fundamentals of heat transfer

The THM coupling in 3DEC involves three distinct heat transfer processes, which are detailed below.

- In the solid domain (rock blocks): Heat is transferred by conduction.
- In the fluid domain (fractures): Heat is transferred by convection, which comprises advection (heat carried by bulk fluid motion) and thermal diffusion (molecular energy exchange).
- At the fluid–solid interface: Heat is exchanged between the fluid in the fractures and the surfaces of the rock blocks.

3.1.1. Heat transfer in the solid domain

Considering a medium with a three-dimensional temperature distribution, the heat transfer vector at a point P on the surface must be perpendicular to the surface and point in the direction of decreasing temperature. The rate of heat conduction at that point can be expressed by Fourier's law as

$$q^T = -k^T \nabla T = -k\left(i\frac{\partial T}{\partial x} + j\frac{\partial T}{\partial y} + k\frac{\partial T}{\partial z}\right) \tag{3.1}$$

where $q^T = (q_x, q_y, q_z)$ is the specific heat flux in rock, k^T is the rock thermal conductivity, i, j, and k are the unit vectors, ∇T represents the temperature gradient. Heat is conducted in the direction of decreasing temperature, and thus the temperature gradient is negative when heat is conducted in positive directions. The energy-balance equation has the form

$$-\nabla \bullet q^T + q_v = \rho c_p \frac{\partial T}{\partial t} \tag{3.2}$$

where $\nabla \bullet q^T$ is first derivative of heat flux representing the divergence of the heat flux vector q^T(i.e., a measure of the rate at which heat is changing). Substituting q^T into the energy-balance equation yields the fundamental energy-balance equation for heat conduction (Forsberg 2021)

$$k^T \nabla^2 T + q_v = \rho c_p \frac{\partial T}{\partial t} \tag{3.3}$$

where $\nabla^2 T = \nabla \bullet (\nabla T)$ is the second partial derivative of the temperature field T, representing the Laplacian. The parameter q_v is the volumetric heat source representing the rate at which heat is generated per unit volume within the material, ρ is the density, and c_p is the specific heat capacity at constant pressure.

In the coupled THM model, this generic source term q_v is specifically defined as the heat exchanged with the fluid at the fracture interface. Therefore, the specific form of the energy-balance equation solved for the solid blocks in 3DEC is:

$$\rho_s c_s \frac{\partial T_s}{\partial t} + \nabla \bullet q_s^T - A_s h\left(T_f - T_s\right) = 0 \tag{3.4}$$

where $\rho_s c_s$ is the solid density times specific heat (the solid heat capacity), q_s^T is the heat flux in the solid (from Eq. (3.1), A_s is the contact area per unit volume of solid, and the final term $-A_s h\left(T_f - T_s\right)$ represents this specific heat source/sink from the interaction with the fluid.

3.1.2. Heat transfer in the fluid domain

Fluid flow rates through fractures are significantly higher than through pores in intact rock, making matrix flow in crystalline rock negligible. Therefore, fluid flow in the rock mass is primarily controlled by the fractures, only considering the hydraulically active fracture network. In the fluid domain (the fractures), heat is transferred by convection, which describes the transport of thermal energy via the fluid flow and is a combined process consisting of advection (the transport of heat by the bulk motion of the fluid) and thermal diffusion (the molecular exchange of energy, which in the 3DEC implementation is modeled as conduction). Both of these processes are captured in the full energy-balance equation for the fluid.

Assuming that fluid flow occurs within fluid-saturated fractures, and that the rock matrix is impermeable to fluid flow, the thermal diffusion (conduction) component of the heat flux q_f^T is defined by Fourier's law:

$$q_f^T = -k_f^T \nabla T \tag{3.5}$$

where k_f^T is fluid thermal conductivity. The full energy-balance equation for the fluid combines this diffusion term with the advection term and the heat exchange at the solid–fluid interface:

$$\rho_f c_f \frac{\partial T_f}{\partial t} + \nabla \bullet q_f^T + \rho_f c_f q^f \bullet \nabla T_f + A_f h\left(T_f - T_s\right) = 0 \tag{3.6}$$

where $\rho_f c_f$ is the product of fluid density and specific heat, q^f is the specific fluid discharge (the fluid flow rate per unit area), and ∇T_f is the fluid temperature gradient. The parameter A_f is the contact area per unit fluid volume, h is the fluid/rock heat transfer coefficient, and T_f and T_s are temperature of fluid and solid block, respectively. This equation accounts for the change in energy ($\rho_f c_f \frac{\partial T_f}{\partial t}$), the heat transfer by conduction/diffusion ($\nabla \bullet q_f^T$), the heat transfer by advection ($\rho_f c_f q^f \bullet \nabla T_f$), and the heat exchange with the solid ($A_f h\left(T_f - T_s\right)$).

3.1.3. Heat transfer at the fluid–solid interface

At the fluid-rock boundary, heat is transferred from the fluid to the rock matrix or vice versa. Heat transfer between the fluid inside the fractures and the contacting rock (fluid-thermal coupling) may take place according to Newton's law of cooling, which is given by (Itasca 2022)

$$q_n = h(T_b - T_e) \tag{3.7}$$

where q_n is the component of the flux normal to the boundary in the direction of the exterior normal, h is the convective heat-transfer coef-

ficient, T_b is the temperature of the boundary surface, and T_e is the temperature of the surrounding fluid.

3.2. Fundamentals of fluid flow in 3DEC fractures

The governing equations for fluid flow in contacts follow a simplified form of the Navier-Stokes equation. Considering fluid flow between two nearly parallel, impermeable boundaries (plates) in combination with incompressibility of the fluid, the simplified Reynolds equation is obtained. This implies no net change in mass flux through the control volume

$$\frac{\partial}{\partial x}\left(\frac{b^3\rho g}{12\eta}\frac{\partial h}{\partial x}\right)+\frac{\partial}{\partial y}\left(\frac{b^3\rho g}{12\eta}\frac{\partial h}{\partial y}\right)=0 \tag{3.8}$$

where b is the distance between the impermeable boundaries at some point (x, y) in the plane, $h=z+p/\rho g$ is the hydraulic head, z is the elevation, p is the fluid pressure, g is the acceleration due to gravity, ρ is the fluid density, and η is the dynamic fluid viscosity. The equation demands that flow is laminar. The fluid flow rate per unit width q_f [m^3/(m·s)] can be written as

$$q_f=-\frac{\rho g b^3}{12\eta}\nabla h \tag{3.9}$$

where η is the dynamic viscosity [Pa·s], ∇h is the dimensionless hydraulic gradient [m/m]. The mass conservation principle of continuity equation in has a general differential form of (Pedlosky 1987)

$$\frac{\partial\rho}{\partial t}+\nabla\bullet(\rho\boldsymbol{v})=0 \tag{3.10}$$

For flow in a fracture, the specific fluid discharge (flow rate per unit width of the fracture) $q=u\boldsymbol{v}$, and $\boldsymbol{v}$ is the velocity field of the fluid, and u is the fracture aperture, then the continuity equation becomes

$$\frac{\partial(\rho u)}{\partial t}+\nabla\bullet(\rho q)=0 \tag{3.11}$$

For slightly compressible fluids, the density varies with pressure according to

$$K_w=\frac{-\partial p}{(\partial V/V)}=\frac{\partial p}{(\partial\rho/\rho)} \tag{3.12}$$

where K_w is the bulk modulus of fluid. The rate of change of density with time can be expressed as:

$$\frac{\partial\rho}{\partial t}=\frac{\rho}{K_w}\frac{\partial p}{\partial t} \tag{3.13}$$

The total mass within the fracture is given by the product ρu. Substituting it into the mass conservation equation and expanding $\frac{\partial(\rho u)}{\partial t}$:

$$u\left(\frac{\rho}{K_w}\frac{\partial p}{\partial t}\right)+\rho\frac{\partial u}{\partial t}+\nabla\bullet(\rho q)=0 \tag{3.14}$$

Divide through by constant ρ, the continuity equation for a slightly compressible fluid in a deformable rock fracture becomes

$$\nabla\bullet q=-\frac{\partial u}{\partial t}-\frac{u}{K_w}\frac{\partial p}{\partial t} \tag{3.15}$$

where $\nabla\bullet q$ is the divergence of the flow rate, u is the fracture aperture. Combining this with the fluid flow rate equation and assuming η does not vary as a function of position, we obtain the expression

$$\frac{\partial p}{\partial t}=\frac{u^2K_w}{12\eta}\nabla^2p-\frac{K_w}{u}\frac{\partial u}{\partial t} \tag{3.16}$$

where p is fluid pressure [Pa], and ∇^2p is the Laplacian of the pressure [Pa/m^2]. This equation represents the diffusion of pressure within the fracture. In a general case, the fracture aperture u depends on local fracture stiffness, fluid pressure, and mechanical response of the surrounding rock mass. Therefore, the term $\frac{K_w}{u}\frac{\partial u}{\partial t}$ acts as a "source" term, determined by the coupling between fluid flow and mechanical deformation of the solid. This term accounts for the pressure change in the water trapped within the rock fracture due to the deformation of the rock mass and the fractures.

3.3. THM interactions

Thermal effects on rock deformation require the reformulation of the incremental stress–strain relations. This is achieved by subtracting from the total strain increment the portion due to temperature changes. For deformable blocks, the constitutive equation of thermo-elasticity is applied. The total strain consists of two components; (i) the mechanical strain caused by external forces and gravity, and (ii) the thermal strain increments caused by temperature gradients (Itasca 2022; Tiedtke et al. 2024).

$$\Delta\varepsilon_{ij}=\Delta\varepsilon_{ij}^{M}+\Delta\varepsilon_{ij}^{T},\ \text{and} \tag{3.17}$$

$$\Delta\varepsilon_{ij}^{T}=\alpha_T\Delta T\delta_{ij} \tag{3.18}$$

where δ_{ij} is the Kronecker delta. For an isotropic material, the thermal stress due to temperature change is derived from the principles of thermo-elasticity:

$$\Delta\sigma_{ij}^{T}=-3K\alpha_T\Delta T\delta_{ij} \tag{3.19}$$

where α_T is the linear thermal expansion coefficient and ΔT is the temperature increment. The negative sign indicates that an increase in temperature (expansion) results in compressive thermal stress if the material is constrained. The thermal expansion or contraction of the rock matrix alters the aperture and normal stress of contacts, and the thermal stresses induced in the matrix lead to stress redistributions. These thermal effects are coupled with the behavior of the contacts, as represented in the newly developed contact model.

When a rock fracture is filled with fluid under a certain pressure, the normal deformation of the fracture is influenced by a linear combination of the confining pressure (or total normal stress) in the rock, σ_n, and the fluid pressure, p_p. This combination produces what is termed an "effective stress" σ_n'

$$\sigma_n'=\sigma_n+\alpha p_p \tag{3.20}$$

where α is the Biot effective stress coefficient of the fracture (Selvadurai 2019; Suvorov and Selvadurai 2019). Since pore pressure directly counteracts the normal stress acting on a smooth fracture without roughness (note that a mixed-sign convention is used in 3DEC: while the mechanical solver is compression-positive, the fluid-coupling formulation is tension-positive, where σ_n is negative in compression; thus, the positive p_p correctly reduces the magnitude of the compressive stress), it is generally assumed that $\alpha=1$ (Itasca 2022; De Simone et al. 2023). The hydraulic aperture is a measure of the effective opening of a fracture through which fluid can flow. In general, the hydraulic aperture is defined as

$$u_h=u_{h0}+\Delta u_n \tag{3.21}$$

where u_{h0} is the hydraulic aperture at zero stress, Δu_n is the joint normal displacement (positive denoting opening), representing the aperture or width of the fracture when no external stress is applied.

3.4. THM parameters for crystalline rock model

Material properties based on datasets of crystalline rock parameters

reported in the literature (Wang and Konietzky 2019; Tiedtke et al. 2024) are used to demonstrate the relevance and applicability of the model to a wide range of crystalline rock scenarios. These parameters are selected to reflect the general behavior of crystalline rocks. The block and contact properties are not tailored to any specific rock, but are designed to represent the typical behavior of generic crystalline rocks. This approach aligns with the objective of this research, aiming to develop a broadly applicable model for crystalline rock formations. The parameter set used for modelling is summarized in Table 1. By incorporating these input parameters, the 3DEC model simulates the THM coupling effectively by capturing interactions between fluid pressure, thermal effects, and mechanical responses within fractures.

3.5. Model limitations and simplifications

The numerical framework employed in this study incorporates specific geometric and physical simplifications to balance model complexity with computational efficiency at the reservoir scale. Structurally, the rock mass is represented as an assemblage of convex polyhedral blocks separated by planar discontinuities. Consequently,

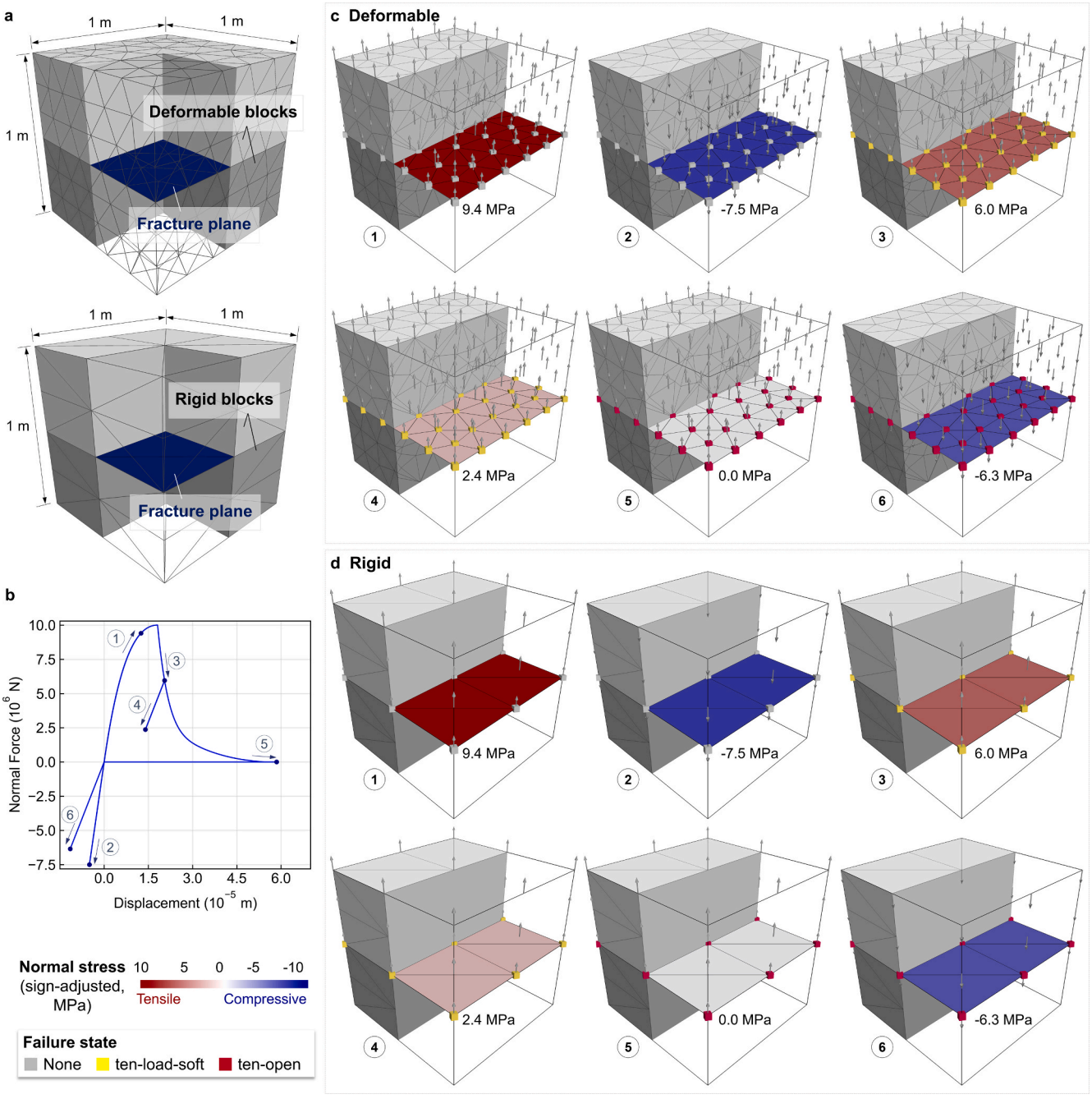

Fig. 3. Test of the proposed contact model using a cubic model with a single fracture plane. (a) Constructed model using deformable and rigid blocks with fracture planes lying within each of them. (b) Force-displacement curve experienced by the model, with arrows and numbers indicating the loading path. For consistency and direct comparison with the curve, the numerical stress results adopting a compression-positive convention were sign-adjusted (i.e., multiplied by –1) in this figure. (c) Deformable model and (d) rigid model at six loading stages, with color boxes indicating failure states ("ten" denotes tension failure, "load" denote the loading stage, "soft" denotes the softening stage, "open" denotes the fully open of the crack), and arrows indicating displacement vectors. The residual cohesion c_{res} is set as 0.5c in this cubic model to prevent the premature occurrence of slip states.

fractures are restricted to these predefined contact planes, and propagation occurs exclusively along existing boundaries. Since the joints behave according to constitutive laws applied at contacts without representing intra-block microcracking, the fracture geometry is idealized as planar, and secondary micro-fracturing within the blocks is not explicitly modeled.

Furthermore, the thermal and hydraulic models involve specific simplifications, and the thermal and hydraulic formulations rely on specific assumptions regarding matrix permeability. The crystalline rock matrix is assumed to be impermeable to fluid flow; thus, fluid transport occurs exclusively within the fracture network. As a consequence of this zero-matrix-flow assumption, heat transfer within the solid blocks is modeled solely via conduction, neglecting advective heat transport through the rock matrix pores. Heat exchange between the fluid and the solid is therefore restricted to the fracture–matrix interface. Despite these simplifications, this approach provides a robust and computationally feasible means of simulating progressive cracking and heat extraction in large-scale geothermal reservoirs.

4. Model validation under different THM conditions

4.1. Model with single fracture plane

A single fracture plane within a cube (1 m × 1 m × 1 m) is constructed in order to check the successful implementation of the newly proposed contact constitutive model, as shown in Fig. 3a. Both rigid and deformable blocks are created to validate the new model development and implementation. The bottom block is fixed, preventing translation and rotation, while a constant displacement rate is applied to the upper block to conduct direct tensile tests (without lateral confinement). For a clear illustration of the force–displacement curve (see Fig. 3b) during loading and re-loading, λ_u is set to 3 in these cube models. Fig. 3 presents the force–displacement behaviors for both deformable and rigid block systems at various stages of loading, unloading, and reloading. Fig. 3b shows the force–displacement curve, while Fig. 3c and Fig. 3d visualize the block movements and fracture stress distributions at key moments in the process. Initially, during tensioning, the model exhibits elastic behavior, but as damage progresses, a reduction in stiffness becomes evident in the pre-failure stage. With ongoing loading, the tensile strength is exceeded, transitioning the model into the softening phase. During this phase, unloading and subsequent reloading are simulated. As the model unloads during softening, a noticeable reduction in stiffness (i.e., the decayed stiffness) occurs. When reloading begins, the force–displacement curve first follows the path of unloading, then merges back with the original loading curve once the displacement reaches the point where unloading commenced. As displacement reaches the critical value u_c, the fracture opens fully, allowing the upper block to move without resistance (stress-free). When compressed back to its original position, the model exhibits a reduced stiffness in subsequent compressive stages as well. The simulation results demonstrate that the newly proposed contact constitutive model effectively captures both elastic and softening behaviors during loading–unloading-reloading processes (as illustrated in Fig. 1), irrespective of whether the blocks are deformable or rigid, showing its robustness in handling complex repeated heating–cooling induced load cycles in the context of geothermal storage and extraction procedures.

4.2. Thermo-mechanical (TM) coupling

To verify temperature distribution and thermal-induced stresses, we adopted the classic model of a hollow cylinder of infinite length, exposed to different temperatures at its inner and outer curved surfaces (Fig. 4d), using the analytical solution provided by (Nowacki 1986) and the built-in Mohr-Coulomb model in 3DEC (Itasca 2022). The temperature distribution and radial, tangential, and axial stresses at the thermal steady-state are given by the following equations

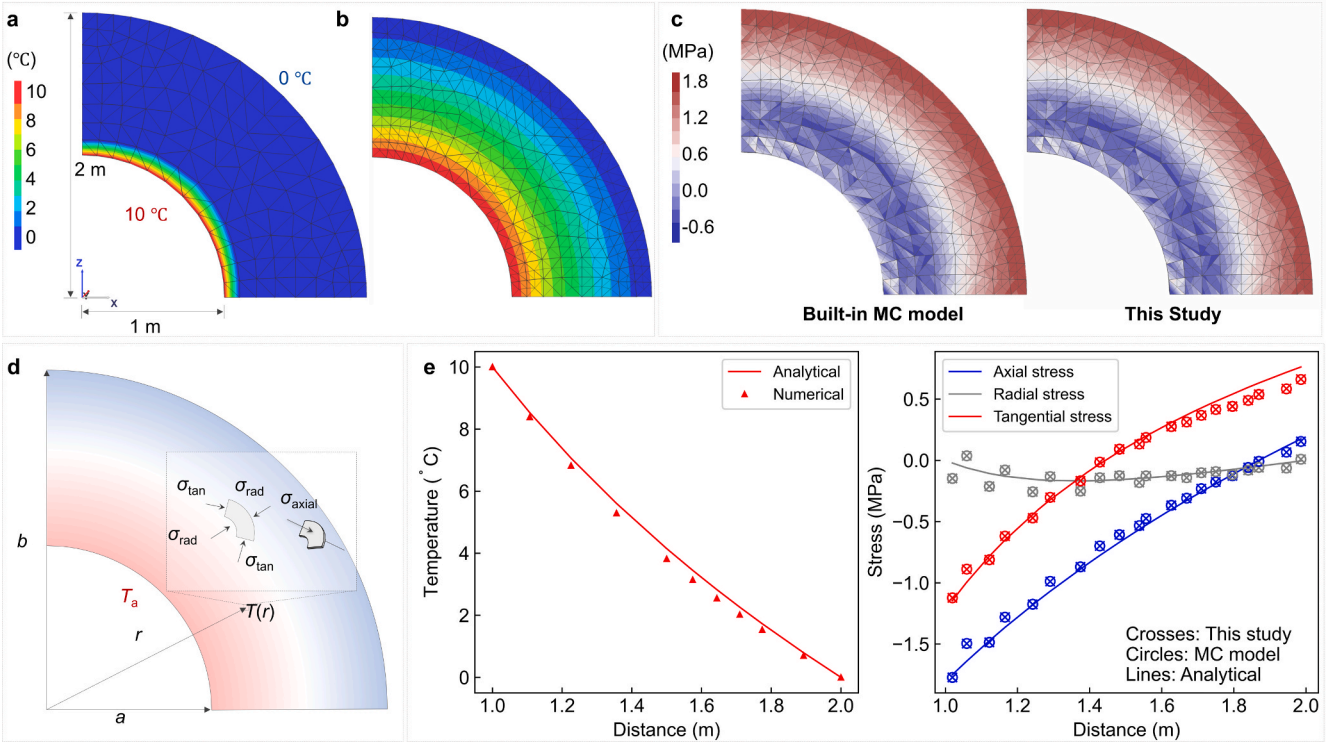

Fig. 4. (a) Geometry and boundary conditions of the hollow cylinder model. Temperature distribution (b) and maximum principal stress (c) of the model at steady thermal conduction state. (d) Theoretical model for temperature and stress distribution at steady thermal conduction state. (e) Analytical solutions (lines) and numerical results (symbols) of temperature and stresses distribution, among the symbols: triangles for temperature profile, crosses for this study, circles for the built-in Mohr-Coulomb model.

$$T(r) = \frac{\ln(b/r)}{\ln(b/a)} T_a \tag{4.1}$$

$$\sigma_{rad}(r) = -\frac{3\alpha_T G T_a K}{\lambda + 2G}\left[\frac{\ln(b/r)}{\ln(b/a)} - \frac{(b/r)^2 - 1}{(b/a)^2 - 1}\right] \tag{4.2}$$

$$\sigma_{tan}(r) = -\frac{3\alpha_T G T_a K}{\lambda + 2G}\left[\frac{\ln(b/r) - 1}{\ln(b/a)} + \frac{(b/r)^2 + 1}{(b/a)^2 - 1}\right], \text{ and} \tag{4.3}$$

$$\sigma_{axial}(r) = -\frac{3\alpha_T G T_a K}{\lambda + 2G}\left[\frac{2\ln(b/r) - \frac{\lambda}{2(\lambda+G)}}{\ln(b/a)} + \left(\frac{\lambda}{2\lambda + G}\right)\frac{2}{(b/a)^2 - 1}\right] \tag{4.4}$$

where, T is the temperature distribution, r is the radial distance from the cylinder center, a is the inner radius of the cylinder, b is the outer radius of the cylinder, T_a is the temperature at the inner radius, σ_{rad} is the radial stress, σ_{tan} is the tangential stress, σ_{axial} is axial stress, K is the bulk modulus, G is the shear modulus, α_T is the linear thermal expansion coefficient, and $\lambda = K - 2G/3$ is a material constant.

The cylinder has an inner radius of 1.0 m and an outer radius of 2.0 m, as shown in Fig. 4a, with boundary temperatures set at 10 ℃ and 0 ℃, respectively. The simulation results for steady thermal conduction are presented in Figs. 4b and 4c. Since both models produce the same temperature distribution, only one temperature profile is shown in Fig. 4b. The maximum principal stress distributions show nearly no difference between the proposed model and the built-in Mohr-Coulomb model. For a more quantitative comparison, Fig. 4e presents the simulated results of both temperature and stress distributions alongside the analytical solutions. The proposed model demonstrates strong agreement with analytical solutions on radial stress at the inner boundary, tangential stress at the outer boundary, and axial stress near the inner boundary. Although the model shows a 0.34 % higher error in tangential stress than the Mohr-Coulomb model, it reduces axial and radial stress errors by 0.11 % and 0.16 %, respectively. These minor discrepancies, which are comparable to those observed in the 3DEC built-in model, validate the accuracy, stability, and robustness of the newly developed contact model for thermo-mechanical (TM) simulations. Furthermore, they confirm the successful integration of the new model into 3DEC, demonstrating its capability to perform in TM coupling scenarios.

4.3. Hydro-mechanical (HM) coupling

Rock formations may experience fracture extension when pressurized viscous fluid is injected into the deep fractured rock mass. For instance, during the injection of fluid into a fractured geothermal system, the fluid pressure can cause extension of pre-existing fractures. To verify the accuracy and capability of the proposed model in simulating such hydro-mechanical behavior, the Perkins–Kern–Nordgren (PKN) model (Perkins and Kern 1961) is adopted for comparison (see Fig. 5). The PKN model provides an analytical description of a vertically constrained hydraulic fracture propagating under plane-strain conditions, and fluid pressure is assumed uniform across each horizontal cross-section. It establishes relationships between the fracture width, net pressure, and injection parameters based on elasticity and lubrication theory. The built-in Mohr-Coulomb model is also compared with the newly implemented cohesive model. The fracture is assumed to have a fixed height H, and the fluid pressure is constant in vertical elliptical cross-section perpendicular to the direction of propagation. The corresponding 3DEC model (Itasca 2022) is illustrated in Fig. 5, featuring graded mesh, with the finest discretization of 1 m zone size near the fracture and the coarsest discretization of 4 m zone size away from the fracture along the far-field boundaries. The net pressure p_{net} at the crack tip is zero since the fracturing fluid pressure is equal to confining stress. The net pressure can be approximated using the following expression (Itasca 2022)

$$p_{net} = \left[\frac{16\eta q E^3}{(1-\nu^2)\pi H^4} L\right]^{1/4} \tag{4.5}$$

while the expression for the width (aperture) in the middle of the fracture is

$$w(x) = 3\left[\frac{\eta q (1-\nu^2)(L-x)}{E} L\right]^{1/4} \tag{4.6}$$

where q is the injection rate, η is the viscosity of the injected fluid, L and H are the length and height of the fracture, respectively.

The 3DEC model geometry is constructed based on the symmetry of the problem, representing only the upper half of the fracture. The fracture trace is predefined by a vertical contact plane, initially joined but allowed to open (fracture) within a constant-height layer during the simulation, driven by stress changes induced by the injected fluid. The granite matrix has extremely low permeability and is considered impermeable compared with fractures. The fluid domain is represented explicitly by the predefined fracture plane, and flow within each fracture follows the cubic law. After 300 s of injection at a rate of 2×10^{-3} m^3/s, the simulation results are compared with the PKN solution. Fig. 6a displays fluid pressure and fracture aperture contours extending from the injection point to the fracture tip. Pressure and aperture contours of

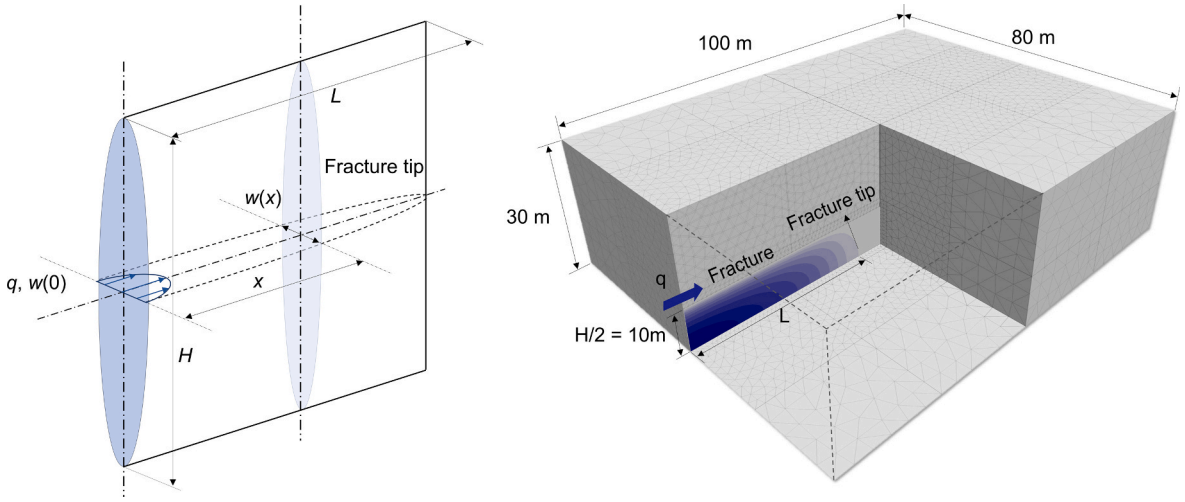

Fig. 5. Geometry of PKN model and 3DEC PKN model (modified from (Itasca 2022)).

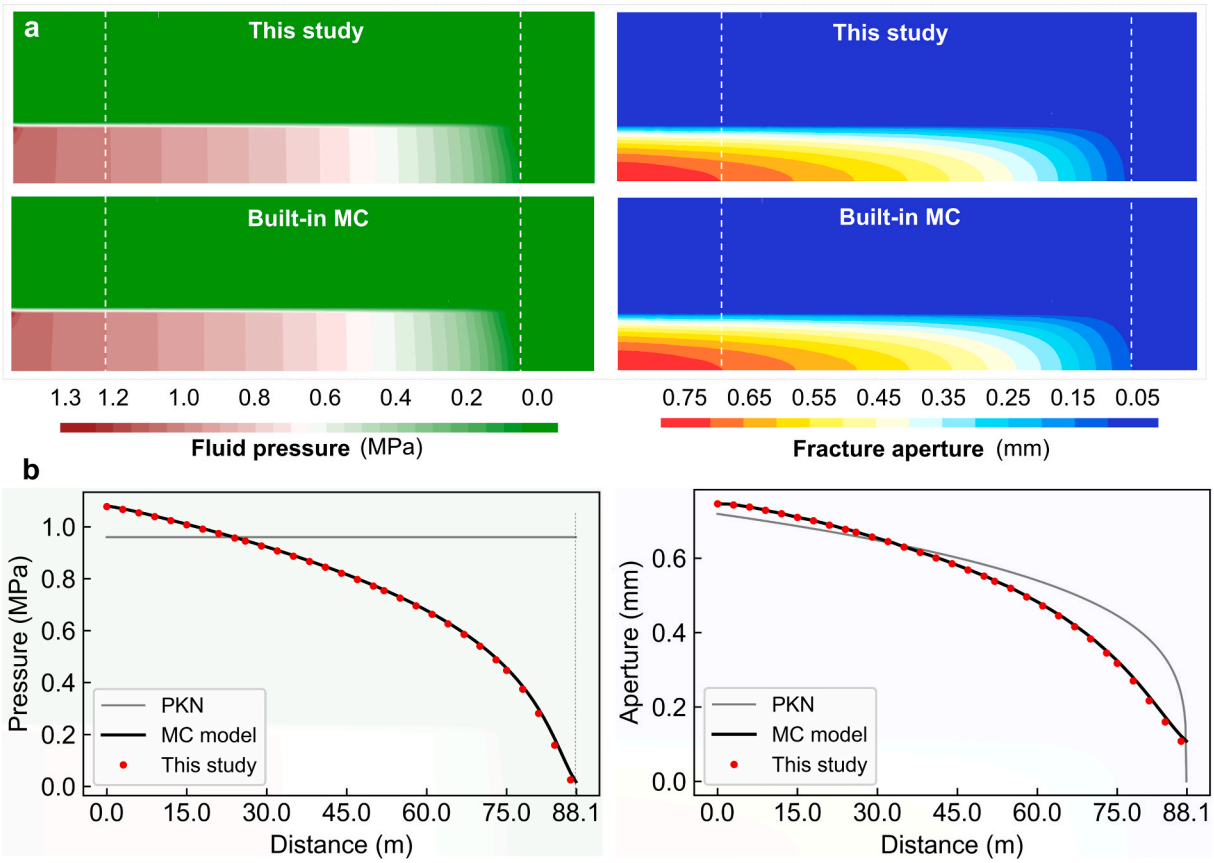

Fig. 6. (a) Comparison of fluid pressure and fracture aperture contours between the built-in Mohr-Coulomb model and the model proposed in this study. Vertical white dashed lines are added as reference markers to visualize the slight discrepancies in distribution between the two models. (b) Quantitative comparison of simulated fluid pressure and fracture aperture against PKN analytical solutions (grey line); results from this study are shown as red dots, and the built-in Mohr-Coulomb model results are shown as a solid black line.

the new model align closely with the simulated results of the built-in Mohr-Coulomb model. In Fig. 6b, these simulated results are quantitatively compared with the PKN solutions. The match in maximum widths is particularly accurate near the injection point, but discrepancies arise near the fracture tip. This is due to the use of constant strain zones in 3DEC, which inadequately approximate the stress singularity and strain gradients at the tip. Additionally, there is a residual aperture in 3DEC to prevent model instability as the aperture decreases to zero (Itasca 2022), which is set to 50 μm in this work. This constraint also contributes to the less accurate match near the fracture tip. Overall, the numerical solutions are in reasonably good agreement with the PKN solutions. At the injection point, the built-in Mohr-Coulomb model shows a 12.5 % error in net pressure compared to the PKN solutions, while the proposed model has a slightly lower error of 12.3 %. For fracture width, the Mohr-Coulomb model and the proposed model exhibit errors of 3.9 % and 3.8 %, respectively. The proposed model demonstrates good agreement with the PKN solutions, showing slightly better accuracy than the built-in Mohr-Coulomb model verifying the successful implementation of the new contact model for H-M coupled calculations.

Fig. 7 presents the simulation results of the progressive cracking process during fluid injection. The models employing the two different contact models exhibit similar displacement distributions in the fracture plane. The proposed contact model with default λ_u captures the totally opened fracture (indicated by the 'ten-open' failure states) and a softening transition (indicated by 'ten-load-soft' failure states) of less than 2 m along the fracture tip. As λ_u increases from 1.27 to 2.0, the maximum width of the softening transition area expands to about 5 m, while the distance from injection point to fracture tip remains unchanged. Additionally, the fracturing extent after the same injection duration is smaller in the proposed model compared to the Mohr-Coulomb model. The most significant advantage of the new model lies in its ability to sophisticatedly simulate the progressive evolution of failure states from the injection point to the fracture tip during the injection process. Unlike the built-in Mohr-Coulomb model, which only indicates whether a fracture occurs, the proposed model captures the dynamic transition along the fracture plane. It shows a fully opened state near the injection point, a softened state towards the fracture tip, and partial micro-cracks ahead of the tip.

This capability is important for crystalline rock geothermal storage and extraction systems, where the failure states of fractures can vary significantly. Such variations influence fracture morphology, mechanical properties, and thermo-elastic responses, all of which play a crucial role in THM coupling during heat storage and extraction. By accurately simulating the progressive fracturing process, the new model enables a more sophisticated assessment of fracture behavior. This contributes to a deeper understanding of its role in geothermal systems and supports improved evaluations of heat production performance.

4.4. Effects of repeated heating–cooling on the behavior of hydraulic fractures

Hydraulic injection is commonly used to create multifracture systems in geothermal reservoirs. During the thermal energy storage and extraction process, these fractures are subjected to repeated heating and cooling cycles. To investigate the model applicability of replicating this phenomenon, a simplified 3D model is built as illustrated in Fig. 8. The model has dimensions of 1.25 m × 0.5 m × 0.5 m, with a predefined weak fracture plane located horizontally at the mid-height of the domain

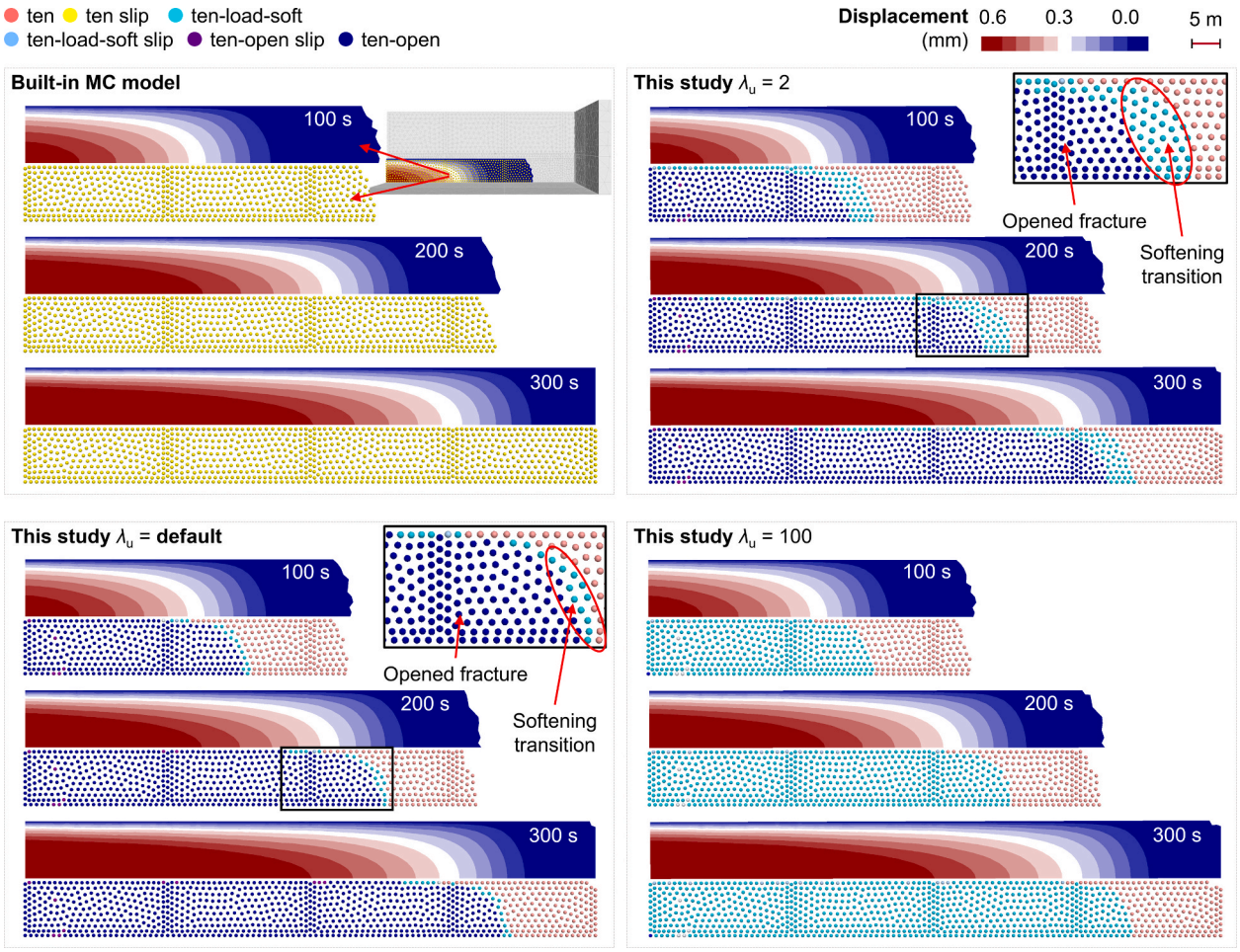

Fig. 7. Progressive failure of the fracture plane – comparison between the built-in Mohr-Coulomb model and the newly proposed models with different λ_u (i.e., default $\lambda_u = u_c/(u_c - 6.324G_{IC}/f_t) = 1.27$, self-defined $\lambda_u = 2$, self-defined $\lambda_u = 100$). ("ten" denotes tension failure, "slip" denotes shear failure, "load" denotes the loading stage, "soft" denotes the softening stage, "open" denotes the fully open of the crack).

and a width of 0.2 m. A vertical normal stress of 1 MPa is applied to the top surface, while all other boundaries are fixed in their normal directions. As documented previously in Section 4.3, both the built-in Mohr-Coulomb (MC) model and the newly proposed cohesive crack model are applied for comparison. The model parameters are consistent with those used in Fig. 7, and the initial temperature is set to 20 °C.

Hydraulic flow is injected to create an initial fracture. Following this, the model is subjected to four heating–cooling cycles under two different temperature scenarios (Fig. 8): Scenario 1 reaches a peak temperature of 50 °C, while Scenario 2 reaches 150 °C. The performance of the built-in MC model and the proposed model is compared based on Scenario 1, ensuring all other settings remain identical. Furthermore, Scenario 2 is applied exclusively to the newly proposed model to evaluate the influence of higher maximum temperatures, as such variations are often employed in engineering practice to enhance system performance.

4.4.1. Comparison with standard Mohr-Coulomb model

Initially, hydraulic fracturing creates a fracture length of 0.397 m in the MC model, which is very close to the 0.401 m predicted by the new model. However, the MC model is limited to indicating binary failure states (either tensile or shear slip), whereas the new model captures the sophisticated fracturing process including initiation, post-peak loading & unloading softening, and full opening. After the first heating cycle (HT1), the fracture length in the MC model increases to 0.480 m, while the new model predicts an extension to 0.485 m, showing a slight difference of 0.005 m. However, this divergence becomes more pronounced after the fourth heating and cooling cycle: the MC fracture extends only slightly to 0.486 m, while the new model predicts a final length of 0.503 m. Although the absolute values differ, both models confirm that thermal cycling significantly influences hydraulic fracture propagation. The critical disadvantage of the standard MC model is its inability to capture the progressive degradation of joint stiffness and strength during the heating–cooling reversals (loading–unloading–reloading). In contrast, the newly proposed model successfully simulates the complex opening and closing behaviour associated with these thermal cycles, demonstrating a significant advantage in capturing the fatigue-like damage accumulation observed in crystalline rocks.

4.4.2. Impact of temperature scenarios

Using the newly developed model, the results show that in Scenario 1 (50 °C), the hydraulic fracture extends from 0.401 m to 0.485 m during the first heating phase. In Scenario 2 (150 °C), the fracture length increases significantly to 0.638 m. For the subsequent second to fourth heating cycles, both scenarios still show fracture growths but with the increments being much smaller than during the first heating phase. During the cooling phases, the fracture length in Scenario 1 remains nearly unchanged. In Scenario 2, minor reductions are observed during the fourth cooling phase, indicating that cooling has a significantly smaller impact on fracture propagation compared to heating. After four full cycles, the final fracture length reaches 0.503 m in Scenario 1 and 0.717 m in Scenario 2, clearly demonstrating the strong influence of maximum injection temperature on fracture evolution. In addition to length extension, repeated thermal cycling also increases the range of

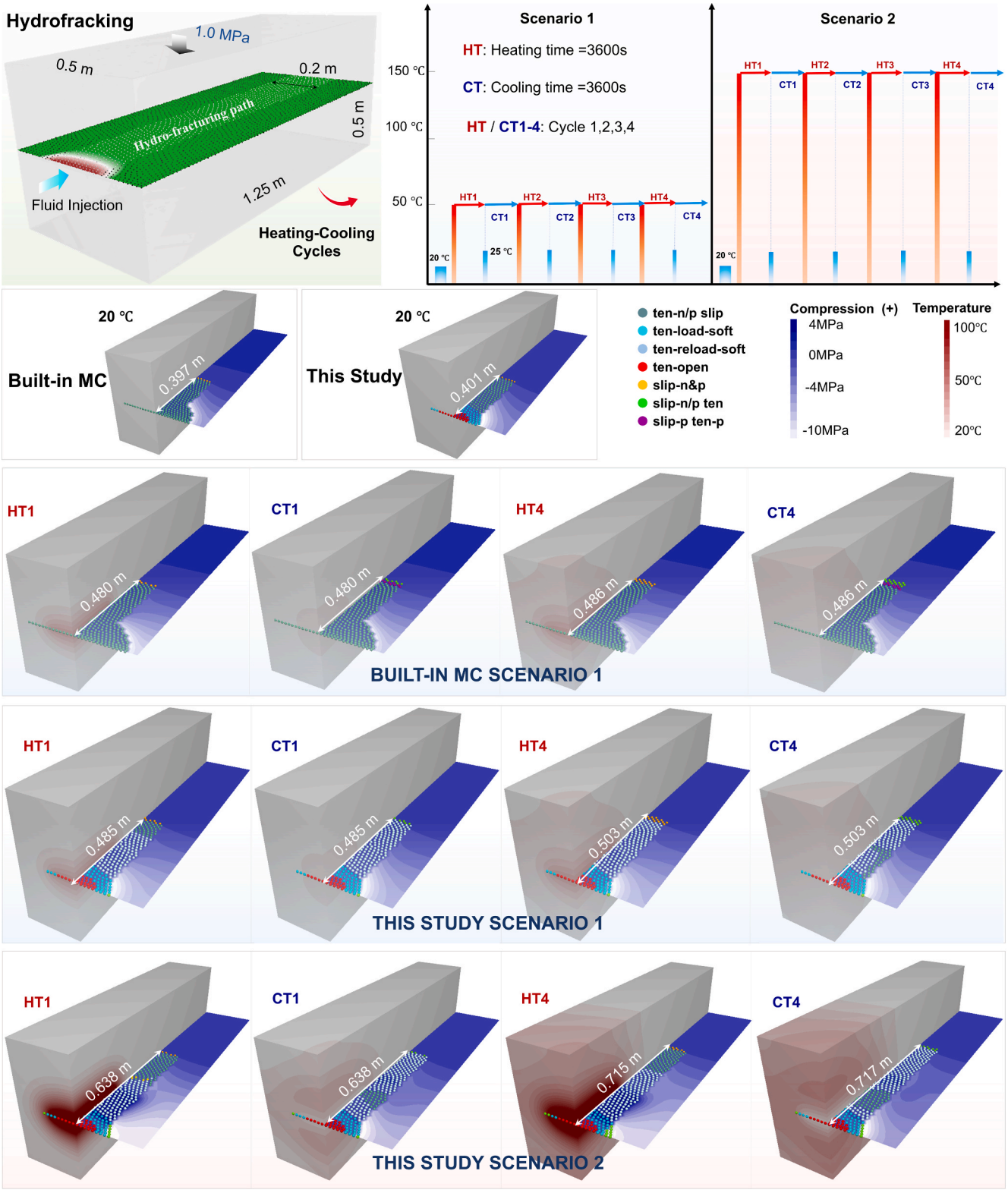

Fig. 8. Effects of repeated heating–cooling cycles on the development of hydraulic fractures: A comparison between the built-in Mohr-Coulomb (MC) model and the newly developed cohesive crack model. Results are presented for 1st and 4th heating/cooling cycles under two temperature scenarios. (Legend: "ten" denotes tension failure, "slip" denotes shear failure, "n/p" denotes now/past, "load" denotes the loading stage, "soft" denotes the softening stage, "open" denotes the fully open of the crack).

reactivated or reloaded fracturing, suggesting that the fractures undergo loading–unloading–reloading processes throughout the thermal cycles.

These findings highlight the importance and applicability of the newly developed cohesive contact model. The proposed model not only accommodates a variety of thermo-hydro-mechanical (THM) coupling conditions but also excels in simulating the progressive and cyclic nature of fracture evolution under complex loading histories in geothermal systems.

5. Conclusions

This paper introduces a new cohesive cracking model to simulate the progressive fracturing behavior of crystalline rocks under THM conditions such as in FTES. The model employs a nonlinear stress-displacement relationship and a softening function governing post-peak tensile stress reduction. The successful implementation of this model in 3DEC significantly expands the software's capability for simulating the progressive fracturing behavior of crystalline rocks under various conditions.

One of the major innovations of this model lies in its flexible parameterization. The two softening parameters c_1 and c_2 define the shape of the post-peak softening curve and can be tailored to capture different rock softening behaviors, while the displacement-scaling coefficient λ_u adjusts the critical crack opening according to rock type, element size, and thermo-hydraulic conditions. This allows the model to reproduce a wide spectrum of fracturing behaviors observed in crystalline rocks under diverse thermal and hydraulic environments.

The model's accuracy and robustness were verified against analytical and experimental benchmarks. In the thermo-mechanical (TM) validation, the model reproduced the analytical solution for a hollow cylinder with a maximum stress deviation of less than 0.13 MPa (radial) and 0.10 MPa (tangential), while reducing axial stress errors by 0.11 % compared to the standard Mohr-Coulomb model. In hydro-mechanical (HM) fracturing simulations, the proposed model achieved a fracture width error of 3.8 % and a net pressure error of 12.3 % relative to the analytical PKN solution. This demonstrates slightly better accuracy than the built-in Mohr-Coulomb model, which exhibited errors of 3.9 % and 12.5 %, respectively. Furthermore, in the application to geothermal reservoirs under cyclic thermal loading, the model quantified the significant impact of temperature on fracture evolution: increasing the peak injection temperature from 50 °C to 150 °C resulted in a 42.5 % increase in the final fracture length (from 0.503 m to 0.717 m) after four cycles. These results confirm the model's capability to capture complex, progressive fracturing behaviors with high quantitative accuracy.

By capturing the entire fracture evolution, from crack initiation and post-peak softening to full crack opening, the model effectively simulates complex failure modes, especially in scenarios where tensile behavior predominates. The model's ability to simulate the dynamic interactions between fractures, heat flux, and fluid flow provides valuable insights into the stability and performance of underground geothermal reservoirs. Its application can be extended beyond geothermal energy storage systems, offering potential benefits in fields such as underground storage, hydraulic fracturing, and traditional rock mechanics research.

CRediT authorship contribution statement

Fei Wang: Writing – original draft, Visualization, Software, Project administration, Methodology, Investigation, Funding acquisition, Formal analysis, Conceptualization. **Dehao Meng:** Writing – original draft, Visualization, Investigation, Formal analysis. **Heinz Konietzky:** Writing – review & editing, Software, Resources, Formal analysis. **Eleni Gerolymatou:** Writing – review & editing, Methodology, Formal analysis. **Paul W.J. Glover:** Writing – review & editing, Methodology. **Ben-Guo He:** Writing – review & editing, Funding acquisition.

Declaration of competing interest

The authors declare that they have no known competing financial interests or personal relationships that could have appeared to influence the work reported in this paper.

Acknowledgments

This work was partially supported by the National Natural Science Foundation of China (Nos. W2431040 and 52222810). The first author also gratefully acknowledges the support of the Alexander von Humboldt Foundation.

Data availability

Data will be made available on request.

References:

Bongole, K., Sun, Z., Yao, J., et al., 2019. Multifracture response to supercritical CO2-EGS and water-EGS based on thermo-hydro-mechanical coupling method. Int. J. Energy Res. 43, 7173–7196. https://doi.org/10.1002/er.4743.

Broberg, K.B., 1971. Crack-growth criteria and non-linear fracture mechanics. J. Mech. Phys. Solids 19, 407–418. https://doi.org/10.1016/0022-5096(71)90008-1.

Cao, Y., Xu, J., Chen, L., et al., 2020. Experimental study on granite acoustic emission and micro-fracture behavior with combined compression and shear loading: phenomenon and mechanism. Sci. Rep. 10, 22051. https://doi.org/10.1038/s41598-020-78137-0.

Cornetti, P., Muñoz-Reja, M., Sapora, A., Carpinteri, A., 2019. Finite fracture mechanics and cohesive crack model: Weight functions vs. cohesive laws. Int. J. Solids Struct. 156–157, 126–136. https://doi.org/10.1016/j.ijsolstr.2018.08.003.

De Simone, S., Darcel, C., Kasani, H.A., et al., 2023. Equivalent Biot and Skempton Poroelastic Coefficients for a Fractured Rock Mass from a DFN Approach. Rock Mech. Rock Eng. 56, 8907–8925. https://doi.org/10.1007/s00603-023-03515-9.

Farahmand, K., Diederichs, M., 2015. Implementation of a Cohesive Crack Model in Grain-based DEM Technique for Simulating Fracture in Quasi-Brittle Geomaterial. In Proceedings of the 68th Canadian Geotechnical Conference and the 7th Canadian Permafrost Conference. Quebec City.

Farahmand, K., Diederichs, M.S., 2021. Calibration of coupled hydro-mechanical properties of grain-based model for simulating fracture process and associated pore pressure evolution in excavation damage zone around deep tunnels. J Rock Mech Geotech 13, 60–83. https://doi.org/10.1016/j.jrmge.2020.06.006.

Forsberg, C.H., 2021. Chapter 2 - Heat conduction equation and boundary conditions. In: Forsberg, C.H. (Ed.), Heat Transfer Principles and Applications. Academic Press, pp. 23–55.

Gdutos, E., 2020. Fracture mechanics: an introduction, Third edition. Springer, Cham.

Hesselbrandt, M., Acuna, J., 2022. Modeling and performance evaluation of fractured thermal energy storage (FTES). International Ground Source Heat Pump Association. International Ground Source Heat Pump Association, Las Vegas.

Hillerborg, A., Modéer, M., Petersson, P.-E., 1976. Analysis of crack formation and crack growth in concrete by means of fracture mechanics and finite elements. Cem. Concr. Res. 6, 773–781. https://doi.org/10.1016/0008-8846(76)90007-7.

Huang, Y., Zhang, Y., Gao, X., Ma, Y., 2022. Thermal disturbance analysis in rock-soil induced by heat extraction from the abandoned well. Geothermics 101, 102374. https://doi.org/10.1016/j.geothermics.2022.102374.

Itasca (2022) 3DEC — Three-Dimensional Distinct Element Code.

Janiszewski, M., 2019. Techno-economic aspects of seasonal underground storage of solar thermal energy in hard crystalline rocks. Aalto University. Doctoral Thesis.

Janssen, M., Zuidema, J., Wanhill, R., 2004. Fracture Mechanics, 2nd Edition. Spon Press, London, UK.

Kazerani, T., 2013. Effect of micromechanical parameters of microstructure on compressive and tensile failure process of rock. Int. J. Rock Mech. Min. Sci. 64, 44–55. https://doi.org/10.1016/j.ijrmms.2013.08.016.

Kazerani, T., Yang, Z.Y., Zhao, J., 2012. A Discrete Element Model for predicting Shear Strength and Degradation of Rock Joint by using Compressive and Tensile Test Data. Rock Mech. Rock Eng. 45, 695–709. https://doi.org/10.1007/s00603-011-0153-6.

Kazerani, T., Zhao, J., 2014. A Microstructure-based Model to Characterize Micromechanical Parameters Controlling Compressive and Tensile failure in Crystallized Rock. Rock Mech. Rock Eng. 47, 435–452. https://doi.org/10.1007/s00603-013-0402-y.

Koltzer, N., Bott, J., Bär, K., Scheck-Wenderoth, M., 2023. How temperatures derived from fluid flow and heat transport models impact predictions of deep geothermal potentials: the "heat in place" method applied to Hesse (Germany). Geotherm. Energy 11, 2. https://doi.org/10.1186/s40517-023-00245-7.

Kumar, S., Barai, S.V., 2009a. Effect of softening function on the cohesive crack fracture parameters of concrete CT specimen. Sadhana 34, 987–1015. https://doi.org/10.1007/s12046-009-0059-0.

Li, S., Zhang, D., 2023. Three-Dimensional Thermoporoelastic Modeling of Hydrofracturing and Fluid Circulation in Hot Dry Rock. J. Geophys. Res. Solid Earth 128, e2022JB025673. https://doi.org/10.1029/2022JB025673.

Liu, C., Zhang, Q., Xiang, W., Zhou, X., 2020. Experimental Study on Characteristics and Mechanism of Macrography and Mesoscopic failure of Deep Granite from Beishan. Geotech. Geol. Eng. 38, 3815–3830. https://doi.org/10.1007/s10706-020-01260-2.

Liu, J., Chen, L., Wang, C., et al., 2014. Characterizing the mechanical tensile behavior of Beishan granite with different experimental methods. Int. J. Rock Mech. Min. Sci. 69, 50–58. https://doi.org/10.1016/j.ijrmms.2014.03.007.

Liu, P., Liu, Q., Deng, P., et al., 2024. A Novel Mixed-Mode Power Exponent Cohesive Zone Model for FDEM and its Application to Tunnel Excavation in the Layered Rock Mass. Rock Mech. Rock Eng. 57, 1219–1243. https://doi.org/10.1007/s00603-023-03599-3.

Nowacki, W., 1986. Thermoelasticity, 2nd ed., rev.enl. Pergamon Press PWN-Polish Scientific Publishers, Oxford New York Warszawa.

Okubo, S., Fukui, K., 1996. Complete stress-strain curves for various rock types in uniaxial tension. Int J Rock. Mech. Min. Sci. & Geomech. Abstr. 33, 549–556. https://doi.org/10.1016/0148-9062(96)00024-1.

Pedlosky, J., 1987. Geophysical fluid dynamics. Springer-Verlag, New York.

Perkins, T.K., Kern, L.R., 1961. Widths of Hydraulic Fractures. J. Petrol. Tech. 13, 937–949. https://doi.org/10.2118/89-PA.

Perng, J.-D., 1989. Analysis of crack propagation in asphalt concrete using a cohesive crack model. The Ohio State University, Master.

Planas, J., Elices, M., Guinea, G.V., et al., 2003. Generalizations and specializations of cohesive crack models. Eng. Fract. Mech. 70, 1759–1776. https://doi.org/10.1016/S0013-7944(03)00123-1.

Preisig, G., Eberhardt, E., Gischig, V., et al., 2015. Development of connected permeability in massive crystalline rocks through hydraulic fracture propagation and shearing accompanying fluid injection. Geofluids 15, 321–337. https://doi.org/10.1111/gfl.12097.

Reinhardt, H.W., Cornelissen, H.A.W., Hordijk, D.A., 1986. Tensile Tests and failure Analysis of Concrete. J. Struct. Eng. 112, 2462–2477. https://doi.org/10.1061/(ASCE)0733-9445(1986)112:11(2462).

Saadat, M., Taheri, A., 2020. Modelling micro-cracking behaviour of granite during direct tensile test using cohesive GBM approach. Eng. Fract. Mech. 239, 107297. https://doi.org/10.1016/j.engfracmech.2020.107297.

Selvadurai, A.P.S., 2019. The Biot coefficient for a low permeability heterogeneous limestone. Contin. Mech. Thermodyn. 31, 939–953. https://doi.org/10.1007/s00161-018-0653-7.

Suvorov, A.P., Selvadurai, A.P.S., 2019. The Biot coefficient for an elasto-plastic material. Int. J. Eng. Sci. 145, 103166. https://doi.org/10.1016/j.ijengsci.2019.103166.

Tatone, B., 2014. Investigating the evolution of rock discontinuity asperity degradation and void space morphology under direct shear. University of Toronto. Doctoral Thesis.

Tiedtke, F., Konietzky, H., Magri, F., 2024. A novel DFN-DEM approach to simulate long-term behavior of crystalline rock under effects of glacial climate conditions. Deep Res. Eng. 1, 100002. https://doi.org/10.1016/j.deepre.2024.100002.

Wang, C.S., Liu, J.F., Zhao, Y.W., Han, S.J., 2022. Mechanical properties and fracture evolution process of Beishan granite under tensile state. Bull. Eng. Geol. Environ. 81, 274. https://doi.org/10.1007/s10064-022-02765-1.

Wang, F., Konietzky, H., 2022. Thermal Cracking in Granite during a Heating–Cooling Cycle up to 1000 °C: Laboratory Testing and Real-Time simulation. Rock Mech. Rock Eng. 55, 1411–1428. https://doi.org/10.1007/s00603-021-02740-4.

Wang, F., Konietzky, H., 2019. Thermo-Mechanical Properties of Granite at Elevated Temperatures and Numerical simulation of thermal Cracking. Rock Mech. Rock Eng. 52, 3737–3755. https://doi.org/10.1007/s00603-019-01837-1.

Wang, F., Konietzky, H., Frühwirt, T., et al., 2020. The Influence of Temperature and High-speed heating on Tensile Strength of Granite and the Application of Digital image Correlation on Tensile failure Processes. Rock Mech. Rock Eng. 53, 1935–1952. https://doi.org/10.1007/s00603-019-02022-0.

Wang, F., Konietzky, H., Pang, R., et al., 2023. Grain-based Discrete Element Modeling of Thermo-Mechanical Response of Granite under Temperature. Rock Mech. Rock Eng. 56, 5009–5027. https://doi.org/10.1007/s00603-023-03316-0.

Wang, F., Meng, D., Hu, K., et al., 2024a. Thermo-mechanical Coupling Characteristics of Granite under Triaxial pressures and Ultrahigh heating rates. Comput. Geotech. 167, 106098. https://doi.org/10.1016/j.compgeo.2024.106098.

Wang, F., Pang, R., Konietzky, H., et al., 2024b. Temperature driven real-time weakening and strengthening mechanisms of unconfined granite. Geothermics 119, 102973. https://doi.org/10.1016/j.geothermics.2024.102973.

Wang, K., Liu, Z., Wu, M., et al., 2024c. Experimental study of mechanical properties of hot dry granite under thermal-mechanical couplings. Geothermics 119, 102974. https://doi.org/10.1016/j.geothermics.2024.102974.

Wong, L.N.Y., Guo, T.Y., Lam, W.K., Ng, J.Y.H., 2019. Experimental Study of Cracking Characteristics of Kowloon Granite based on three Mode I Fracture Toughness Methods. Rock Mech. Rock Eng. 52, 4217–4235. https://doi.org/10.1007/s00603-019-01882-w.

Woodman, J., Ougier-Simonin, A., Stavrou, A., et al., 2021. Laboratory Experiments and grain based Discrete Element Numerical Simulations investigating the Thermo-Mechanical Behaviour of Sandstone. Geotech. Geol. Eng. https://doi.org/10.1007/s10706-021-01794-z.

Xu, X.-P., Needleman, A., 1993. Void nucleation by inclusion debonding in a crystal matrix. Modelling Simul. Mater. Sci. Eng. 1, 111. https://doi.org/10.1088/0965-0393/1/2/001.